

pubs.acs.org/cm Article

# Thermal Atomic Layer Etching of CoO, ZnO, Fe<sub>2</sub>O<sub>3</sub>, and NiO by Chlorination and Ligand Addition Using SO<sub>2</sub>Cl<sub>2</sub> and Tetramethylethylenediamine

Jonathan L. Partridge, Jessica A. Murdzek, Virginia L. Johnson, Andrew S. Cavanagh, Andreas Fischer, Thorsten Lill, Sandeep Sharma, and Steven M. George\*



Cite This: Chem. Mater. 2023, 35, 2058-2068

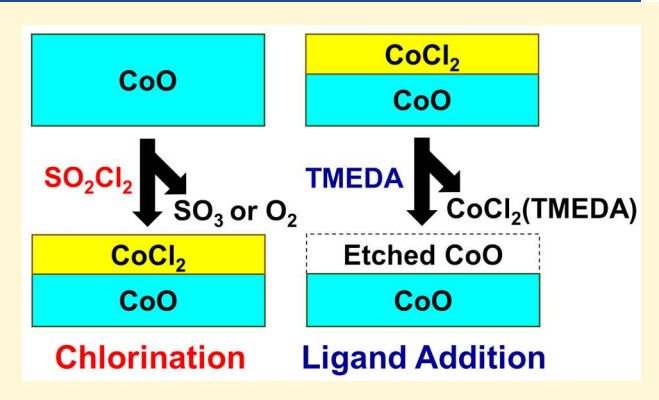


**ACCESS** 

Metrics & More

Article Recommendations

**ABSTRACT:** Thermal atomic layer etching (ALE) of CoO, ZnO, Fe<sub>2</sub>O<sub>3</sub>, and NiO was achieved using chlorination and ligand-addition reactions at 250 °C. This two-step process was accomplished by first chlorinating the metal oxide with  $SO_2Cl_2$ . Subsequently, ligand addition to the metal chloride was performed using tetramethyle-thylenediamine (TMEDA). *In situ* quadrupole mass spectrometry (QMS) studies on metal oxide powders revealed that CoO, ZnO, Fe<sub>2</sub>O<sub>3</sub>, and NiO all formed stable and volatile  $MCl_2(TMEDA)$  compounds (M = Co, Zn, Fe, Ni) as etch products at 250 °C. These QMS studies of the sequential  $SO_2Cl_2$  and TMEDA exposures were facilitated by a new reactor design with two nested inlet lines that transport the reactants separately to the powder substrate. The time-dependence of the reactants and products could also be monitored



by the QMS investigations. The large  $SO_2^+$  ion intensity observed at the beginning of the  $SO_2Cl_2$  exposure was consistent with the chlorination reaction  $MO + SO_2Cl_2 \rightarrow MCl_2 + SO_2 + (1/2)O_2$ . The time-dependent QMS studies also observed the  $MCl_x(TMEDA)^+$  ion intensity peaking at the beginning of the TMEDA exposures. The subsequent decay of the  $MCl_x(TMEDA)^+$  ion intensity, while the  $(TMEDA)^+$  ion intensity remained constant, was evidence for a self-limiting ligand-addition reaction. The mass loss of the metal oxide powders was confirmed after sequential  $SO_2Cl_2$  and TMEDA exposures. The etching of two of these metal oxides was also verified using separate experiments on flat substrates using  $SO_2Cl_2$  and TMEDA exposures at 250 °C. For CoO thermal ALE, an etch rate of 4.1 Å/cycle at 250 °C was measured using X-ray reflectivity (XRR) studies. For ZnO thermal ALE, an etch rate of 0.12 Å/cycle at 250 °C was measured using quartz crystal microbalance (QCM) investigations. Other first row transition metal oxides were surveyed in addition to CoO, ZnO, Fe<sub>2</sub>O<sub>3</sub>, and NiO. QMS studies of TiO<sub>2</sub>, Cr<sub>2</sub>O<sub>3</sub>, and MnO<sub>2</sub> showed no volatile species formation during sequential  $SO_2Cl_2$  and TMEDA exposures at 250 °C. In contrast,  $V_2O_5$  and CuO were spontaneously etched using  $SO_2Cl_2$  at 250 °C, as determined by the observation of volatile VOCl<sub>3</sub> and CuCl<sub>3</sub> etch products, respectively. Calculated Gibbs free energy changes for the various etching reactions also supported the experimental observations for the first row transition metal oxides. These studies illustrate that the chlorination and ligand-addition reaction mechanism can provide a new avenue for the thermal ALE of a variety of transition metal oxides that have nonvolatile metal chlorides.

#### I. INTRODUCTION

Atomic layer etching (ALE) is a highly controllable etch process that utilizes two sequential and self-limiting surface reactions. <sup>1,2</sup> The first reaction modifies the surface, and the second reaction leads to the volatile release of the modified surface layer. <sup>1–3</sup> ALE can be performed using either plasma or thermal methods. <sup>1,2</sup> During plasma ALE, energetic ions or neutrals remove the modified surface layer. <sup>2</sup> During thermal ALE, the modified surface layer is removed by thermal reactions. <sup>1,3</sup>

A variety of thermal ALE pathways have been developed recently.<sup>3</sup> One thermal ALE mechanism is fluorination and ligand exchange.<sup>3-5</sup> During this mechanism, fluorination is

employed as the surface modification step. <sup>6</sup> Ligand exchange is then used to form a volatile etch product. <sup>7–9</sup> This mechanism has been used to etch a variety of metal oxides, including Al<sub>2</sub>O<sub>3</sub>, <sup>4,6,10,11</sup> ZrO<sub>2</sub>, <sup>11,12</sup> and HfO<sub>2</sub>. <sup>11–13</sup> Another thermal ALE mechanism for metal oxides is conversion and volatilization of

Received: December 3, 2022 Revised: February 5, 2023 Published: February 20, 2023





the conversion layer.<sup>3,14</sup> During this mechanism, the metal oxide is first converted to another metal oxide that has a volatile fluoride. The conversion layer is later spontaneously etched by a second thermal fluorination reaction. An example of this conversion mechanism is WO<sub>3</sub> ALE.<sup>14</sup> The surface of WO<sub>3</sub> is converted to a  $B_2O_3$  layer by BCl<sub>3</sub>. HF can then spontaneously remove the  $B_2O_3$  layer.<sup>14,15</sup>

Conversion reactions can also be used to convert one metal oxide into a different metal oxide for subsequent fluorination and ligand-exchange reactions. <sup>16</sup> Examples of this mechanism are ZnO and SiO<sub>2</sub> ALE. <sup>17,18</sup> In these thermal ALE processes, trimethylaluminum (TMA) converts the ZnO or SiO<sub>2</sub> surface to an Al<sub>2</sub>O<sub>3</sub> layer. <sup>17,18</sup> The Al<sub>2</sub>O<sub>3</sub> layer can then be removed by fluorination and ligand exchange. <sup>10</sup> This conversion mechanism can also be extended to Si, SiGe, and Si<sub>3</sub>N<sub>4</sub> ALE by adding an initial oxidation reaction. <sup>19–21</sup> Many other variations on these procedures are possible to etch a variety of oxide and metal materials. For TiN ALE, the TiN surface can first be oxidized to form a TiO<sub>2</sub> surface layer. <sup>22</sup> HF can then spontaneously remove the TiO<sub>2</sub> surface layer by forming a volatile fluoride. <sup>22,23</sup>

Elemental metals can also be etched using thermal ALE. The methods for elemental metals usually proceed by first changing the oxidation number of the metal with oxygen or chlorine reactants. 14,24-27 The resulting metal oxide or metal chloride can then be removed by ligand-substitution or ligand-addition reactions.<sup>24-27</sup> For example, Cu can be etched by first oxidizing the Cu surface to form a copper oxide layer. 26 The copper oxide layer can then be removed by a ligandsubstitution and hydrogen-transfer reaction with Hhfac to form volatile  $\text{Cu}(\text{hfac})_2$  and  $\text{H}_2\text{O.}^{26}$  The thermal ALE of Ni was also demonstrated recently using SO<sub>2</sub>Cl<sub>2</sub> to chlorinate the Ni surface to form NiCl<sub>2</sub>. Exposure to P(CH<sub>3</sub>)<sub>3</sub> then results in ligand addition with NiCl2 to form volatile NiCl<sub>2</sub>(P(CH<sub>3</sub>)<sub>3</sub>)<sub>2</sub> etch products.<sup>27</sup> A variety of group 10 metal chlorides were recently shown to be spontaneously etched by ligand addition with P(CH<sub>3</sub>)<sub>3</sub> to form MCl<sub>2</sub>(P- $(CH_3)_3$ )<sub>2</sub> volatile products.<sup>28</sup>

Based on the demonstration of ligand addition to volatilize metal chlorides, another etching mechanism is possible for metal oxides. The metal oxide can first be chlorinated using a chlorination reactant. The resulting metal chloride can then be volatilized by ligand addition. In this work, the thermal ALE of CoO, ZnO, Fe<sub>2</sub>O<sub>3</sub>, and NiO was developed using SO<sub>2</sub>Cl<sub>2</sub> as a chlorination reactant to convert the metal oxide to a stable, nonvolatile metal chloride. Tetramethylethylenediamine (TMEDA) was then employed as a ligand-addition reactant to remove the metal chloride by forming volatile products. This chlorination and ligand-addition mechanism should provide a valuable complement to the fluorination and ligand-exchange mechanism. In particular, the chlorination and ligand-addition reaction pathway may be necessary for metal oxides that have associated metal fluorides that are not easily volatilized by ligand-exchange reactions.

The thermal ALE of metal oxides is also technologically important. CoO, NiO, and Fe<sub>2</sub>O<sub>3</sub> are oxides of magnetic metals. The etching of these metal oxides may be useful for the fabrication of magnetic devices, such as magnetic tunnel junctions in magnetic random access memory (MRAM).<sup>29,30</sup> Thermal ZnO ALE could also be useful for fabricating ZnO nanostructures for a variety of applications such as gas sensing, solar conversion, and light-emitting diodes.<sup>31</sup>

#### II. EXPERIMENTAL SECTION

**II.A.** Quadrupole Mass Spectrometry (QMS) Studies. Previous QMS studies of volatile etch products during ligand-exchange reactions with metal fluoride powders have utilized a reactor with a single reactant source. <sup>8,9,28</sup> This reactor was designed to allow the etch products to expand into a vacuum and form a molecular beam. This molecular beam then passes through a skimmer and flows into a differentially pumped region for QMS analysis. <sup>8</sup>

For the current studies, a new reactor was built to perform studies with two alternating reactants. Figure 1 shows a schematic of the

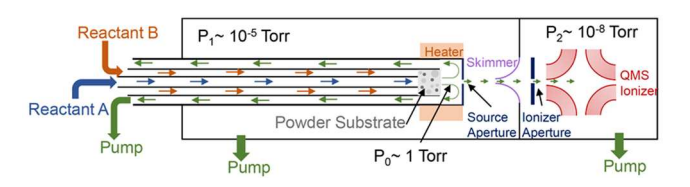


**Figure 1.** Schematic of reactor with two nested gas inlet lines, powder substrate, aperture that allows for molecular beam expansion, and aligned skimmer into a differentially pumped QMS region. Aperture, skimmer, and QMS ionizer are on the same line center.

reactor with two nested gas inlet lines, a powder sample holder, an aperture that allows for molecular beam expansion, and an aligned skimmer into a differentially pumped QMS region. The design of this reactor is similar to the design described previously. A key difference involves the addition of two nested gas lines that allow this reactor to closely model sequential reactant exposures during thermal ALE.

Figure 2 shows a computer-aided design (CAD) schematic of the two nested precursor inlet lines and the gas flow through these gas

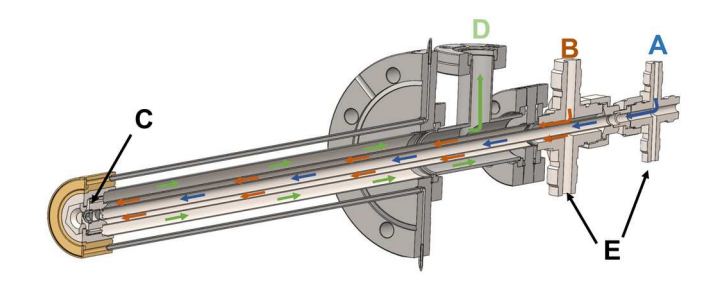


**Figure 2.** Cross-sectional view of the two nested precursor inlet lines and gas flow through these gas lines. (A) Manifold for reactant A gas flow, (B) manifold for reactant B gas flow, (C) heated sample holder containing the powder substrate, (D) gas exhaust, and (E) baratron lines for pressure measurement of each reactant.

lines. The alternating sequential reactant exposures are derived from two separate gas manifolds (A and B in Figure 2). The two separate gas manifolds with nested lines prevent cross-contamination in the chamber by introducing each precursor just upstream of the powder bed (C in Figure 2). This design minimizes the effect of the stainless steel chamber walls and gas lines on the etching reactions.

The volatile species produced by the reaction of reactant gas with the powder bed travel through a 300  $\mu$ m aperture at the end of the sample holder. The etch products and N<sub>2</sub> carrier gas undergo molecular beam expansion. The principle of the molecular beam expansion in this system has been reported elsewhere. The molecular beam was positioned with line-of-sight to the QMS ionizer for high sensitivity detection. After passing through a skimmer, the etch products were analyzed using a quadrupole mass spectrometer (QMS; Extrel MAX-QMS flange-mounted system).

The powders used in these QMS experiments were nanoparticles of CoO (99.7%, US-Nano), ZnO (99.9+%, US-Nano), Fe<sub>2</sub>O<sub>3</sub> (99.5+%, Sigma), NiO (99.5+%, US-Nano), V<sub>2</sub>O<sub>5</sub> (99.95% trace metals basis, Sigma), CuO (high purity 99.95+%, US-Nano), TiO<sub>2</sub> (99.9%, US-Nano), Cr<sub>2</sub>O<sub>3</sub> (99+%, US-Nano), and MnO<sub>2</sub> (ReagentPlus, 99%,

Sigma). Powder masses were weighed before and after the exposure to the ALE reactants to determine material loss. Typical initial powder masses loaded into the sample holder were between 25 and 45 mg. The nanoparticles varied in diameter from 25 to 140 nm. The average particle size for the various nanoparticles was 80 nm.

During the experiments, the combined ultrahigh purity  $N_2$  gas from the two reactant channels flowed through the metal oxide powder at a rate of 4.6 sccm. This  $N_2$  gas flow produced a pressure of  $\approx 3.3$  Torr in the sample holder. The  $N_2$  gas served as both a carrier and purge gas. The partial pressure of  $SO_2Cl_2$  (97%, Sigma-Aldrich) and TMEDA (99%, Sigma-Aldrich) flowing through the metal oxide powder was  $\approx 2.6$  Torr. Sulfuryl chloride is toxic, is corrosive, and releases HCl upon contact with water.  $SO_2Cl_2$  was loaded in a glass bubbler under inert  $N_2$  atmosphere before attachment to the reactor. Experiments were conducted with 120 s exposures of each precursor gas. A purge time of 300 s was employed after the precursor exposures to allow the  $N_2$  gas to purge the powder bed. The temperature of the powder bed was 250 °C for all experiments.

The isotopic distributions of the volatile etch products were calculated from the naturally occurring isotopic abundances of the compound. For example, for FeCl<sub>2</sub>(TMEDA) (TMEDA =  $C_6H_{16}N_2$ ), all four isotopes of Fe ( $^{54}$ Fe,  $^{56}$ Fe,  $^{57}$ Fe,  $^{58}$ Fe), both isotopes of Cl ( $^{35}$ Cl,  $^{37}$ Cl), and all isotopes of C and N in TMEDA were used to generate the expected isotopic patterns. The expected relative abundance was calculated for each m/z value. Some of the m/z values have contributions from more than one distinct species.

II.B. X-ray Reflectivity (XRR) and X-ray Photoelectron Spectroscopy (XPS) Studies. The CoO ALE experiments were performed by measuring the thickness of the CoO films before and after ALE using X-ray reflectivity (XRR). The difference in CoO film thickness before and after CoO ALE yields the CoO thickness change. XRR scans were performed with an X-ray diffractometer (Bede D1, Jordan Valley Semiconductors) using radiation from the Cu K $\alpha$  line at  $\lambda = 1.540$  Å. The X-ray tube filament voltage was 40 kV, and the current was 35 mA. The XRR scan range was 300 to 6000 arcsec with a 5 arcsec step size.

Film thicknesses were determined from the XRR scans using modeling software (REFS, Jordan Valley Semiconductors). The CoO film was prepared utilizing CoO ALD. The initial CoO ALD film had a thickness of between 17 and 22 nm. The CoO ALE experiments were performed at 250 °C using a pulse sequence of SO<sub>2</sub>Cl<sub>2</sub> exposure for 1 s, Ar purge for 120 s, TMEDA exposure for 1 s, and Ar purge for 300 s. During the sequential exposures for CoO ALE, the SO<sub>2</sub>Cl<sub>2</sub> pressure was 140 mTorr and the TMEDA pressure was 40 mTorr. The CoO ALD film was located on top of a film stack composed of 6 nm TiN, on 20 nm SiO<sub>2</sub>, on a silicon wafer.

After CoO ALE, XRR analysis identified an additional layer on top of the CoO film attributed to a porous  $\text{CoO}_x\text{Cl}_y$  material with a thickness of ~7 nm. X-ray photoelectron spectroscopy (XPS) was also performed on this additional layer using an X-ray photoelectron spectrometer (PHI 5600) equipped with a monochromatic Al K $\alpha$  source. The XPS data were analyzed employing CASA XPS (Casa Software Ltd.) software. There was no evidence for sulfur in this top layer.

II.C. Quartz Crystal Microbalance (QCM) Studies. Quartz crystal microbalance (QCM) studies were performed in a viscous flow reactor. <sup>27,33</sup> The reaction temperatures were maintained by a proportional—integral—derivative temperature controller (2604, Eurotherm). A constant flow of ultrahigh purity Ar gas was employed as the carrier and purge gas using mass flow controllers (type 1179A, MKS). A mechanical pump (Pascal 2015SD, Alcatel) was attached at the back of the reactor. The reactor pressure at 1 Torr was maintained using the flowing Ar carrier gas. This pressure was measured by a capacitance manometer (Baratron 121A, MKS).

The quartz crystals (polished, RC cut, gold coated, 6 MHz, Phillip Technologies) were placed in a sensor head (Inficon) and sealed with a high temperature silver epoxy (Epo-Tek H21D, Epoxy Technology Inc.). The QCM head was placed in the isothermal region of the viscous flow reactor. A constant argon gas flow on the back of the QCM was used to prevent deposition of precursors on the backside of

the QCM crystal.  $^{33}$  The changes in resonant frequency of the quartz crystal were recorded and converted to mass using a thin film deposition monitor (Maxtek TM-400, Inficon). The QCM has a precision of  $\sim 1$  ng/cm<sup>2</sup> corresponding to < 1% of one ZnO monolayer. The QCM was left in the reactor at temperature to equilibrate for 12 h before starting experiments.

The ZnO films used for the ZnO thermal ALE studies were grown on the QCM in situ at 200 °C on an Al<sub>2</sub>O<sub>3</sub> ALD film to aid nucleation. The precursors for ZnO ALD were diethyl zinc (DEZ; 52 wt % Zn, Sigma-Aldrich) and water (HPLC grade, submicrometer filtered, Fisher Scientific). The pulse sequence during ZnO ALD was DEZ exposure for 1 s, Ar purge for 30 s, water exposure for 1 s, and Ar purge for 30 s. 100 cycles of ZnO ALD were performed before the ZnO ALE experiments. The ZnO ALE experiments were performed at 250 °C using a pulse sequence of SO<sub>2</sub>Cl<sub>2</sub> exposure for 1 s, Ar purge for 60 s, TMEDA exposure for 1 s, and Ar purge for 300 s. During the exposures, the SO<sub>2</sub>Cl<sub>2</sub> pressure was 140 mTorr and the TMEDA pressure was 40 mTorr. The QCM was allowed to equilibrate in the chamber for 4 h between the ZnO ALD and ZnO ALE experiments.

II.D. Theoretical Methods. All ab initio calculations were performed with Gaussian 16.<sup>34</sup> The Gibbs free energies were calculated for the first-row transition oxides, SO<sub>2</sub>Cl<sub>2</sub> precursor, chlorination products, TMEDA precursor, and TMEDA addition products using a combination of quantum chemical methods and thermochemical methods. The Gibbs free energies of additional species were calculated to explore the experimental observations for vanadium(V) oxide and iron(III) oxide chlorination.

Optimized geometries and vibrational frequencies were calculated at the UB3LYP/sdd level of theory, and single point energies were calculated with UCCSD/sdd.  $^{35-39}$  Translational, vibrational, and rotational degrees of freedom, along with UCCSD single-point energies, were used to calculate the Gibbs free energies at 250  $^{\circ}$ C per established statistical mechanics methods. All reported SO<sub>2</sub>Cl<sub>2</sub> chlorination equations are stoichiometric with respect to one mole of SO<sub>2</sub>Cl<sub>2</sub> to allow for direct comparison between different metal oxide surfaces and reaction products.

#### III. RESULTS AND DISCUSSION

III.A. COO ALE with  $SO_2Cl_2$  and TMEDA. The proposed chlorination and ligand-addition reaction mechanism for CoO ALE is shown in Figure 3. In the first reaction,  $SO_2Cl_2$ 

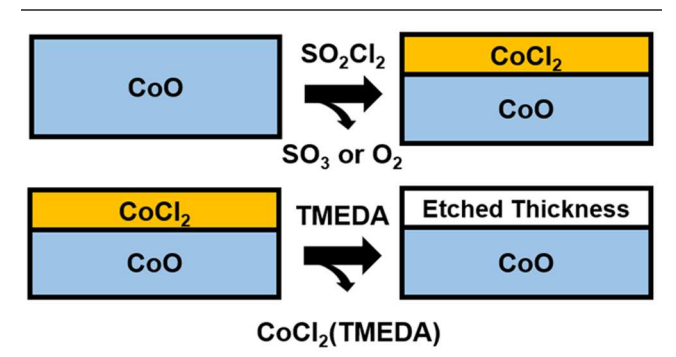
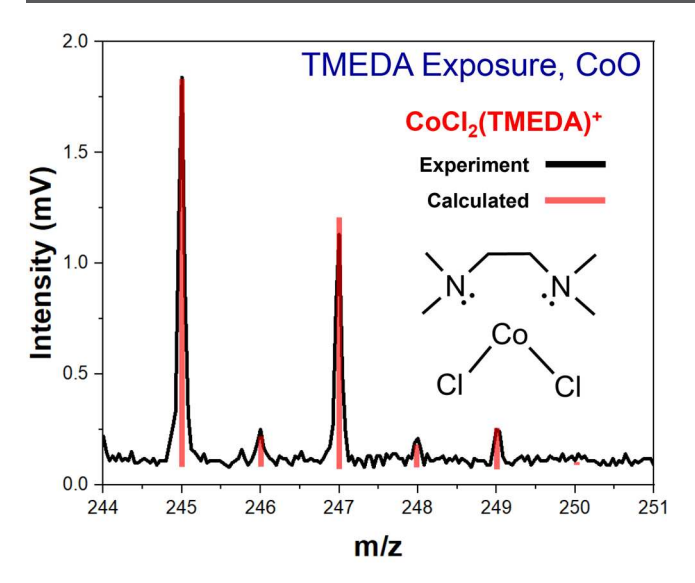


Figure 3. Proposed mechanism for CoO ALE using  $SO_2Cl_2$  for chlorination and TMEDA for ligand addition.

chlorinates the CoO powder to form  $CoCl_2$ . In the second reaction, TMEDA adds to  $CoCl_2$  to form  $CoCl_2$ (TMEDA). To confirm this proposed reaction mechanism, QMS studies were performed during the sequential exposures of  $SO_2Cl_2$  and TMEDA on CoO powder at 250 °C.

Figure 4 shows the QMS ion signal for  $CoCl_2(TMEDA)^+$  observed during a 2.6 Torr TMEDA dose after a previous chlorination reaction with  $SO_2Cl_2$  at 250 °C. The observation



**Figure 4.** Mass spectrum of  $CoCl_2(TMEDA)^+$  from TMEDA exposure on chlorinated CoO at 250 °C. Experimental results are compared with the calculated mass spectrum assuming natural isotopic abundances.

of the  $CoCl_2(TMEDA)^+$  ion intensity argues for TMEDA ligand addition according to the reaction:

$$CoCl_2 + TMEDA \rightarrow CoCl_2(TMEDA)$$
 (1)

as shown in the CoO ALE mechanism given in Figure 3. The isotopic signature for the  $CoCl_2(TMEDA)^+$  ion intensity is in agreement with calculations based on the natural abundance of the various isotopes.

The largest ion signal at m/z 245 is consistent with Co<sup>35</sup>Cl<sub>2</sub>(TMEDA). The second largest ion signal at m/z 247 is attributed to Co<sup>35</sup>Cl<sup>37</sup>Cl(TMEDA). The smaller ion intensity at m/z 249 is assigned to Co<sup>37</sup>Cl<sub>2</sub>(TMEDA). The smallest ion intensities at m/z 246, 248, and 250 are attributed to the natural abundance of the <sup>13</sup>C isotope. Earlier investigations have reported CoCl<sub>2</sub>(TMEDA) with thermal stability up to 300 °C.<sup>32</sup> CoCl<sub>2</sub>(TMEDA) has also been employed as a precursor to deposit CoO ALD films.<sup>32</sup>

When  $SO_2Cl_2$  chlorinates CoO,  $SO_2Cl_2$  is believed to donate chlorine and release  $O_2$  from CoO according to

$$CoO + SO_2Cl_2 \rightarrow CoCl_2 + SO_2 + (1/2)O_2$$
 (2)

This reaction is thermochemically favorable with a free energy change of  $\Delta G = -136.0$  kcal/mol at 250 °C.  $SO_2Cl_2$  could also accept oxygen from CoO and produce  $SO_3$  according to

$$CoO + SO_2Cl_2 \rightarrow CoCl_2 + SO_3$$
 (3)

This reaction is less thermochemically favorable with a free energy change of  $\Delta G = -100.9$  kcal/mol at 250 °C. The experiments reveal that  $SO_3^+$  is not observed at m/z 80 above noise levels during  $SO_2Cl_2$  exposures. However, earlier reports indicate that  $SO_3^+$  is difficult to observe under vacuum conditions. <sup>40</sup> In contrast, the  $SO_2^+$  ion signal may be produced from the electron impact ionization of  $SO_2$ ,  $SO_3$ , or the parent  $SO_2Cl_2$  reactant gas.

Figure 5 shows the time dependence of  $SO_2^+$  and  $SO_2Cl_2^+$  during a  $SO_2Cl_2$  exposure for 120 s. The  $SO_2^+$  ion intensity does not track with the  $SO_2Cl_2^+$  parent ion signal throughout the  $SO_2Cl_2$  exposure. Instead, the first 20 s in Figure 5 show a spike in the  $SO_2^+$  ion intensity prior to the rise of the  $SO_2Cl_2^+$ 

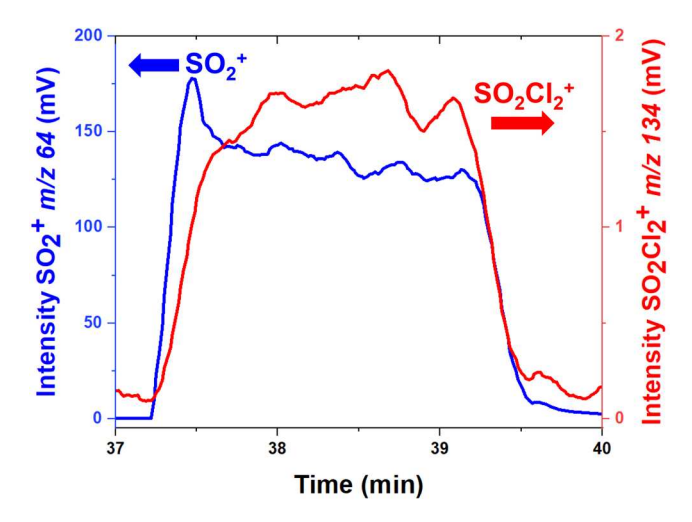


Figure 5. Ion intensity of  $SO_2^+$  and  $SO_2Cl_2^+$  during a 120 s  $SO_2Cl_2$  exposure on CoO at 250  $^{\circ}$ C.

ion intensity. At later times, the  $SO_2^+$  and  $SO_2Cl_2^+$  ion intensities are fairly constant because  $SO_2^+$  is a crack of  $SO_2Cl_2^+$ . This behavior is consistent with  $SO_2Cl_2$  donating 2Cl to form  $CoCl_2$  and releasing  $SO_2$  in the first 20 s.

Other m/z values were analyzed to understand the chlorination of the metal oxide. At m/z 32, similar timeresolved behavior was observed compared with m/z 64 for SO<sub>2</sub><sup>+</sup>. This similarity could indicate either O<sub>2</sub> formation during chlorination or the production of <sup>32</sup>S<sup>+</sup> from the electron impact ionization of SO<sub>2</sub> and SO<sub>2</sub>Cl<sub>2</sub>. The <sup>34</sup>S isotope has an intensity ratio of 4.4% compared with the ion intensity of  $^{32}S^{+}$  at m/z32. The  $^{16}O^{18}O$  isotope at m/z 34 has an intensity ratio of 0.8% compared with the ion intensity of  ${}^{16}O_2^+$  at m/z 32. When comparing the ratio between the ion signal intensities at m/z 34 and m/z 32, the ratio fell as low as 4.2% when most O<sub>2</sub> is proposed to form in the first few seconds of each SO<sub>2</sub>Cl<sub>2</sub> dose. The ratio between the ion signal intensities at m/z 34 and m/z 32 then increased to an average of 4.4% at the end of each SO<sub>2</sub>Cl<sub>2</sub> dose. The ratio falling below 4.4% indicates a mixture of  $O_2^+$  and  $S^+$  formation at m/z 32 during the first few seconds of each SO<sub>2</sub>Cl<sub>2</sub> exposure.

Figure 6 shows the time dependence of the TMEDA<sup>+</sup> and  $CoCl_2(TMEDA)^+$  ion intensities during a TMEDA exposure for 120 s. The TMEDA<sup>+</sup> and  $CoCl_2(TMEDA)^+$  ion intensities both increase at the beginning of the TMEDA exposure. The  $CoCl_2(TMEDA)^+$  ion intensity then decreases, and the TMEDA<sup>+</sup> ion intensity stays constant. The rise and fall of the  $CoCl_2(TMEDA)^+$  ion intensity indicates self-limiting behavior. The  $CoCl_2(TMEDA)$  etch products are produced by the ligand addition of TMEDA with  $CoCl_2$  on the CoO surface. As the  $CoCl_2$  layer is depleted, the  $CoCl_2(TMEDA)$  product also decreases.

In addition to monitoring the etch products, the mass change of the CoO powder was also determined after etching. There was a 48.1% mass loss of the CoO powder after exposure to 5 cycles of SO<sub>2</sub>Cl<sub>2</sub> and TMEDA exposures at 250 °C. An etch rate cannot be obtained quantitatively from the mass loss given the range of particle sizes and varying shapes. To obtain an etch rate for CoO etching using sequential SO<sub>2</sub>Cl<sub>2</sub> and TMEDA exposures, CoO coupons were subjected to alternating cycles of SO<sub>2</sub>Cl<sub>2</sub> and TMEDA exposures at 250 °C.

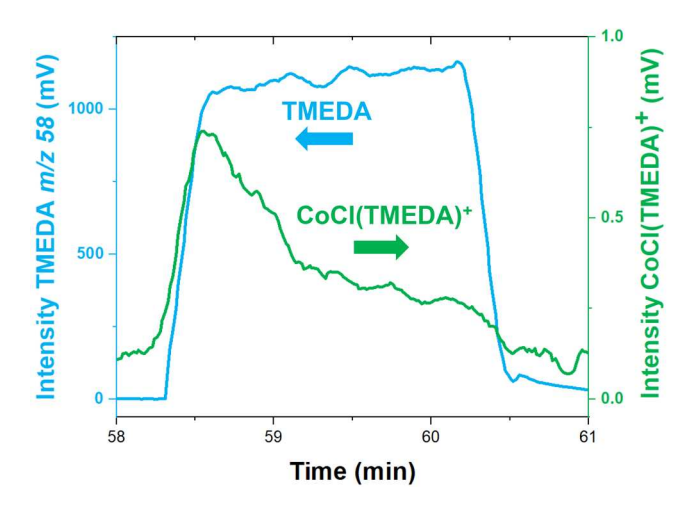


**Figure 6.** Ion intensity of m/z = 58 TMEDA and CoCl<sub>2</sub>(TMEDA)<sup>+</sup> during a 120 s TMEDA exposure on chlorinated CoO at 250 °C.

Figure 7 shows the CoO film thickness change determined by XRR measurements as a function of number of CoO ALE

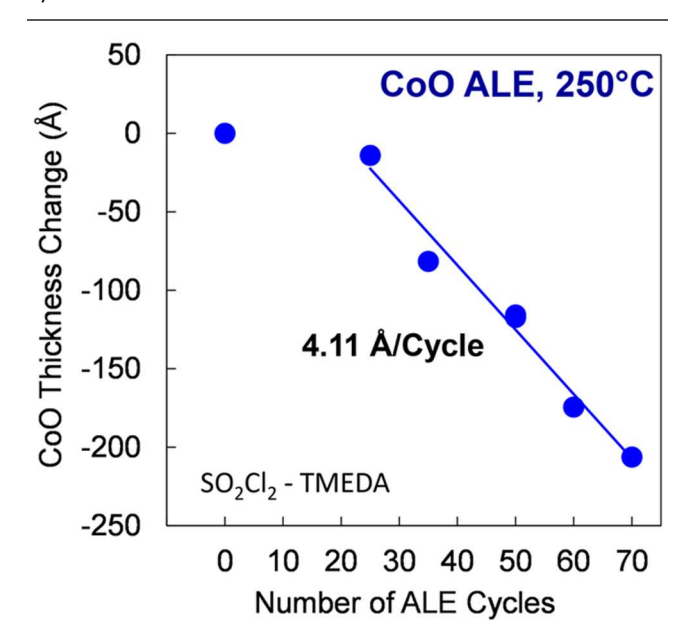


**Figure 7.** CoO thickness change measured by XRR as a function of number of sequential  $SO_2Cl_2/TMEDA$  ALE cycles at 250 °C. Etch rate is 4.11 Å/cycle for the last 45 CoO ALE cycles.

cycles at 250 °C. Each point on the graph corresponds to a new CoO coupon that has been etched for the desired number of ALE cycles. After a short incubation period, the CoO film thickness decreases linearly with the number of ALE cycles. The etch rate is 4.11 Å/cycle for the last 45 CoO ALE cycles. The short etch delay may be caused by surface impurities or surface oxidation because the CoO coupons were prepared in another reactor and exposed to atmosphere prior to loading in the reactor.

III.B. ZnO ALE with  $SO_2Cl_2$  and TMEDA. ZnO ALE can also be performed using sequential  $SO_2Cl_2$  and TMEDA exposures. QMS investigations were conducted to confirm ZnO ALE. For these studies, the ZnO powder was exposed to  $SO_2Cl_2$  and TMEDA at 250 °C. The QMS analysis revealed that  $ZnCl(TMEDA)^+$  ion intensity was the main ion signal

during TMEDA exposures on chlorinated ZnO as shown in Figure 8. No ion intensity was observed for ZnCl<sub>2</sub>(TMEDA)<sup>+</sup>.

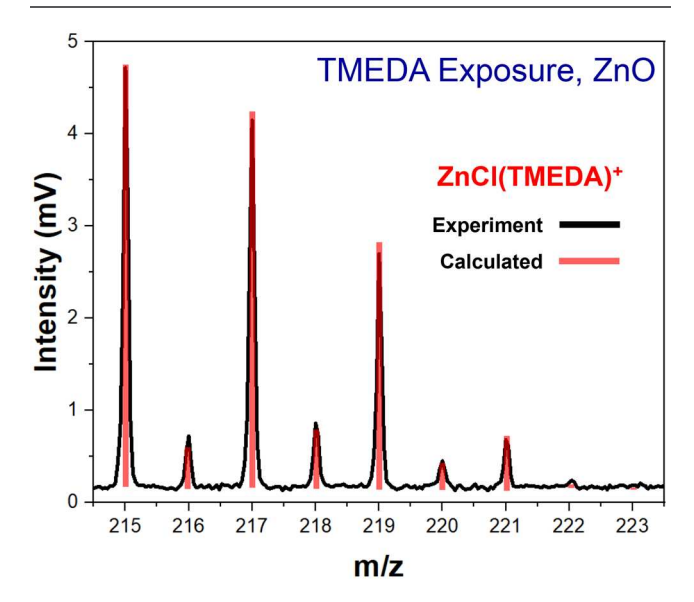


**Figure 8.** Mass spectrum of ZnCl(TMEDA)<sup>+</sup> from TMEDA exposure on chlorinated ZnO at 250 °C. Experimental results are compared with calculated mass spectrum assuming natural isotopic abundances.

Figure 8 confirms the identity of ZnCl(TMEDA)<sup>+</sup> from the observed ion intensities. These ion intensities are in excellent agreement with the calculations based on the Zn, Cl, and C natural isotopic abundances. The largest ion intensity at m/z 215 is consistent with  $^{64}$ Zn $^{35}$ Cl(TMEDA). The second largest ion intensity at m/z 217 agrees with a combination of  $^{64}$ Zn $^{37}$ Cl(TMEDA) and  $^{66}$ Zn $^{35}$ Cl(TMEDA). The third largest ion intensity at m/z 219 is attributed to both  $^{66}$ Zn $^{37}$ Cl(TMEDA) and  $^{68}$ Zn $^{35}$ Cl(TMEDA).

Zn would be in the 1+ oxidation state in a ZnCl(TMEDA) etch product. However, zinc is found almost exclusively as divalent zinc in the 2+ oxidation state. Other Zn(II)TMEDA complexes have been reported including ZnCl<sub>2</sub>(TMEDA). The observation of the ZnCl(TMEDA) ion intensity must indicate that electron impact ionization of ZnCl<sub>2</sub>(TMEDA) yields ZnCl(TMEDA) during QMS analysis. The ZnCl<sub>2</sub>(TMEDA) etch product would be consistent with TMEDA ligand addition to ZnCl<sub>2</sub> and the reaction:

$$ZnCl_2 + TMEDA \rightarrow ZnCl_2(TMEDA)$$
 (4)

The time dependence of the  $SO_2Cl_2$  and TMEDA reactant exposures and the corresponding products can also be monitored using QMS analysis. Figure 9 shows the time-resolved behavior during the  $SO_2Cl_2$  and TMEDA exposures. Figure 9a shows ion intensities for  $SO_2Cl_2^+$  and  $SO_2^+$ . Similar to the behavior in Figure 5, the  $SO_2^+$  ion intensity rises rapidly and peaks prior to the onset of the  $SO_2Cl_2^+$  ion intensity. This behavior again suggests that  $SO_2Cl_2$  donates chlorine to ZnO, releases  $SO_2$ , and produces  $O_2$  from ZnO according to

$$ZnO + SO_2Cl_2 \rightarrow ZnCl_2 + SO_2 + (1/2)O_2$$
 (5)

This reaction is thermochemically favorable with a free energy change of  $\Delta G = -155.6$  kcal/mol at 250 °C.

Another possibility is that  $SO_2Cl_2$  could accept oxygen from ZnO and produce  $SO_3$  according to

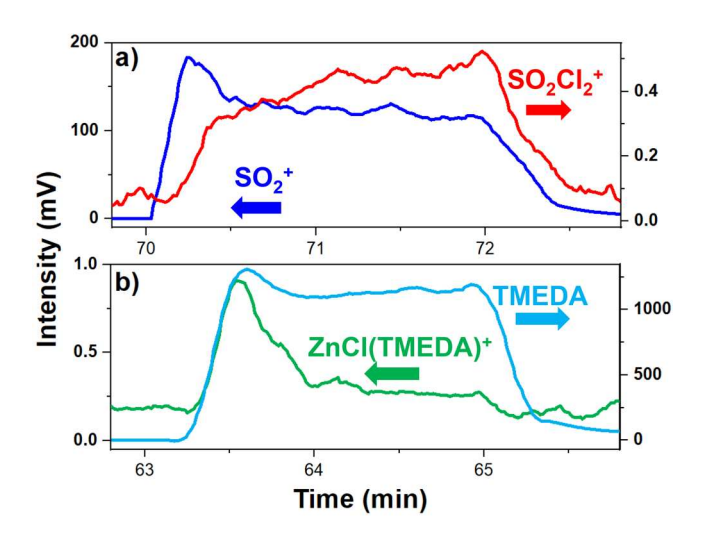


**Figure 9.** (a) Ion intensity of  $SO_2^+$  and  $SO_2Cl_2^+$  during a 120 s  $SO_2Cl_2$  exposure on ZnO at 250 °C. (b) Ion intensity of m/z=58 TMEDA and ZnCl(TMEDA)<sup>+</sup> during a 120 s TMEDA exposure on chlorinated ZnO at 250 °C.

$$ZnO + SO_2Cl_2 \rightarrow ZnCl_2 + SO_3$$
 (6)

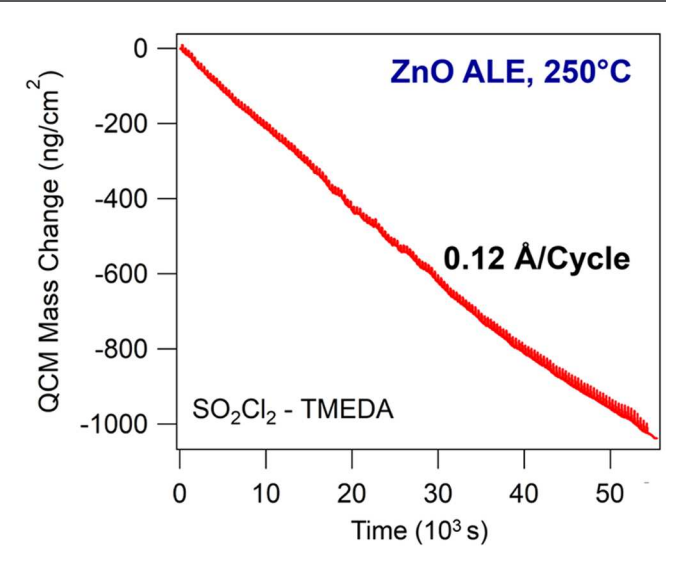
This reaction is less thermochemically favorable with a free energy change of  $\Delta G = -120.5$  kcal/mol at 250 °C. There was also no observation of  $\mathrm{SO_3}^+$  at m/z 80 above noise levels during  $\mathrm{SO_2Cl_2}$  exposures.

Figure 9b shows the time dependence of the ZnCl(TMEDA)<sup>+</sup> ion intensity during a TMEDA exposure. The ZnCl(TMEDA)<sup>+</sup> ion intensity rises concurrently with the TMEDA exposure. This behavior suggests that ligand addition of TMEDA to the chlorinated ZnO surface yields the ZnCl(TMEDA)<sup>+</sup> ion intensity. This ligand addition is self-limiting because there is a finite amount of chlorine on the ZnO surface. As the chlorine species are depleted, the ZnCl(TMEDA)<sup>+</sup> ion intensity decreases accordingly.

The mass of the ZnO powder was also measured before and after the  $SO_2Cl_2$  and TMEDA exposures. There was a 31.3% mass loss of the ZnO powder after 5 cycles of  $SO_2Cl_2$  and TMEDA exposures at 250 °C. QCM measurements were also conducted to confirm ZnO etching. Figure 10 displays QCM results during 150 cycles of ZnO ALE using alternating  $SO_2Cl_2$  and TMEDA exposures. The mass change decreases linearly with time during the sequential  $SO_2Cl_2$  and TMEDA exposures. The etch rate is 6.8 ng/cm²/cycle. This etch rate is equivalent to 0.12 Å/cycle based on the density of 5.62 g/cm³ for ZnO ALD films.  $^{18}$ 

III.C.  $Fe_2O_3$  and NiO Etching with  $SO_2Cl_2$  and TMEDA. Additional experiments were conducted to demonstrate the etching of  $Fe_2O_3$  and NiO using sequential exposures to  $SO_2Cl_2$  and TMEDA. Both  $Fe_2O_3$  and NiO showed volatile ligand-addition species during sequential  $SO_2Cl_2$  and TMEDA exposures at 250 °C. Figure 11 shows the ion intensity for  $FeCl_2(TMEDA)^+$  during a TMEDA exposure at 2.6 Torr after the chlorination of  $Fe_2O_3$  with  $SO_2Cl_2$  at 250 °C. Earlier studies have reported Fe(II)TMEDA compounds including  $FeCl_2(TMEDA)$ .

The isotopic signature of FeCl<sub>2</sub>(TMEDA)<sup>+</sup> is determined predominately by <sup>35</sup>Cl and <sup>37</sup>Cl. As displayed in Figure 11, the agreement is excellent between the experimental results and the calculated intensities based on the natural abundance of the isotopes. The largest ion intensity with an isotopic



**Figure 10.** QCM mass change during ZnO ALE as a function of number of sequential SO<sub>2</sub>Cl<sub>2</sub>/TMEDA ALE cycles at 250 °C. Etch rate is 0.12 Å/cycle using density of 5.62 g/cm<sup>3</sup> for ZnO ALD films.

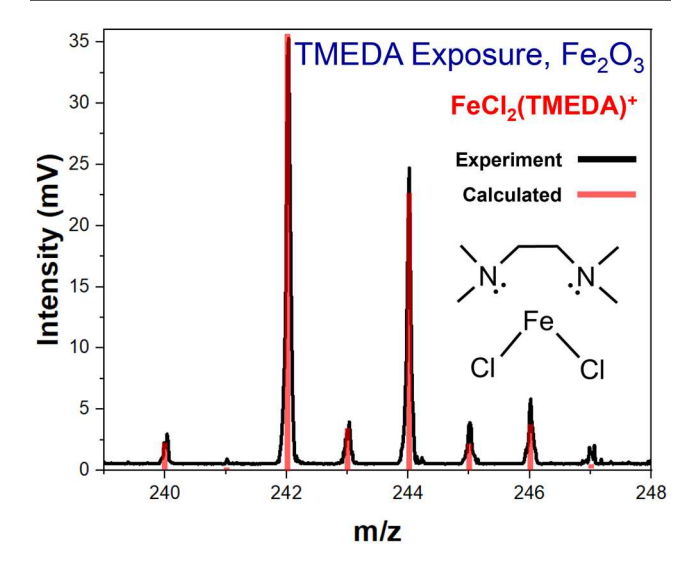


Figure 11. Mass spectrum of  $FeCl_2(TMEDA)^+$  from TMEDA exposure on chlorinated  $Fe_2O_3$  at 250 °C. Experimental results are compared with calculated mass spectrum assuming natural isotopic abundances.

signature at m/z 242 is assigned to  $^{56}\text{Fe}^{35}\text{Cl}_2(\text{TMEDA})$ . The second largest ion intensity at m/z 244 is attributed to  $^{56}\text{Fe}^{35}\text{Cl}^{37}\text{Cl}(\text{TMEDA})$ . Fe has only one isotope with a natural abundance over 5% relative to  $^{56}\text{Fe}$ .  $^{54}\text{Fe}$  with a relative abundance of 6.3% gives rise to the ion intensity for  $^{54}\text{Fe}^{35}\text{Cl}_2(\text{TMEDA})$  at m/z 240.

There is a possibility that some of the measured  $FeCl_2(TMEDA)^+$  ion intensity during QMS analysis could result from  $Fe_2O_3$  on the stainless steel chamber walls. A control experiment was conducted with identical etching conditions in an empty chamber to compare the possible etching of the chamber walls with etching of the  $Fe_2O_3$  powder. The ion intensity of  $FeCl_2(TMEDA)^+$  in an empty chamber with no  $Fe_2O_3$  powder did not exceed 10 mV at m/z 242. The mass loss of the  $Fe_2O_3$  powder also confirmed  $Fe_2O_3$  etching by  $SO_2Cl_2$  and TMEDA. Mass measurements were recorded before and after 5 cycles of alternating  $SO_2Cl_2$  and

TMEDA exposures at 250  $^{\circ}$ C. These mass measurements revealed a mass loss of 36.1%.

The chlorination of Fe<sub>2</sub>O<sub>3</sub> by SO<sub>2</sub>Cl<sub>2</sub> could occur to produce FeCl<sub>3</sub> in the 3+ oxidation state based on the reaction:

$$(1/3)$$
Fe<sub>2</sub>O<sub>3</sub> + SO<sub>2</sub>Cl<sub>2</sub>  $\rightarrow$   $(2/3)$ FeCl<sub>3</sub> + SO<sub>2</sub> +  $(1/2)$ O<sub>2</sub> (7

This reaction is thermochemically favorable with a free energy change of  $\Delta G = -95.6$  kcal/mol at 250 °C. Alternatively, Fe<sub>2</sub>O<sub>3</sub> could be chlorinated by SO<sub>2</sub>Cl<sub>2</sub> to produce FeCl<sub>2</sub> in the 2+ oxidation state according to

$$(1/2)$$
Fe<sub>2</sub>O<sub>3</sub> + SO<sub>2</sub>Cl<sub>2</sub>  $\rightarrow$  FeCl<sub>2</sub> + SO<sub>2</sub> +  $(3/4)$ O<sub>2</sub> (8)

This reaction is thermochemically favorable with a free energy change of  $\Delta G = -70.0$  kcal/mol at 250 °C.

The calculations also explored TMEDA ligand addition to FeCl<sub>3</sub> and FeCl<sub>2</sub> according to

$$FeCl_3 + TMEDA \rightarrow FeCl_3(TMEDA)$$
 (9)

$$FeCl_2 + TMEDA \rightarrow FeCl_2(TMEDA)$$
 (10)

Both reactions are predicted to be thermochemically favorable with a free energy change of  $\Delta G = -64.1$  kcal/mol for FeCl<sub>3</sub>(TMEDA) and  $\Delta G = -88.6$  kcal/mol for FeCl<sub>2</sub>(TMEDA). The experimentally observed FeCl<sub>2</sub>(TMEDA)<sup>+</sup> ion intensity at m/z 242 is consistent with a FeCl<sub>2</sub>(TMEDA) etch product. The FeCl<sub>2</sub>(TMEDA) etch product argues for Fe in the 2+ oxidation state derived from FeCl<sub>2</sub> on the surface. In contrast, a FeCl<sub>3</sub>(TMEDA)<sup>+</sup> ion signal from a FeCl<sub>3</sub>(TMEDA) etch product was not observed at m/z 277.

Similar results were observed for the etching of NiO powder. Figure 12 shows the ion intensities for  $NiCl_2(TMEDA)^+$  during a TMEDA exposure at 2.6 Torr after chlorination of NiO powder with  $SO_2Cl_2$  at 250 °C.  $NiCl_2(TMEDA)$  and similar Ni(II) compounds with different X ligands and TMEDA have been previously reported. In addition to  $NiCl_2(TMEDA)^+$ , there were also ion intensities from Fe

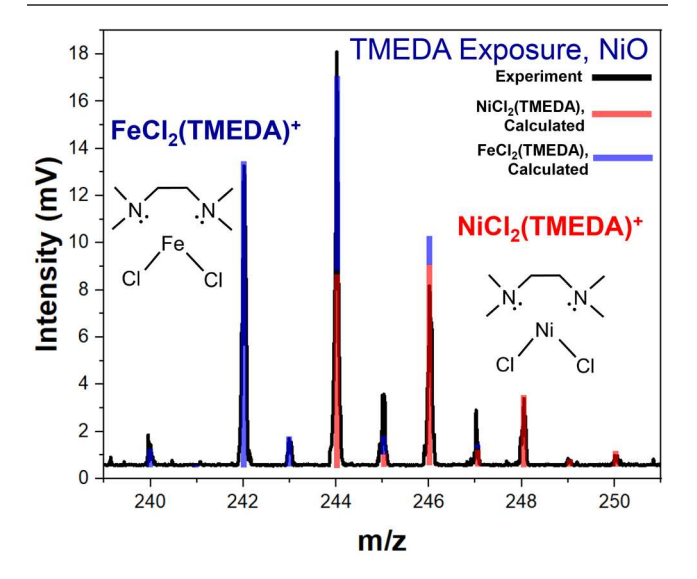


**Figure 12.** Mass spectrum of FeCl<sub>2</sub>(TMEDA)<sup>+</sup> and NiCl<sub>2</sub>(TMEDA)<sup>+</sup> from TMEDA exposure on chlorinated NiO at 250 °C. Experimental results are compared with calculated mass spectrum assuming natural isotopic abundances.

species during these experiments with NiO powder. Figure 12 reveals the ion intensity for  $FeCl_2(TMEDA)^+$  with similar magnitude to the  $NiCl_2(TMEDA)^+$  ion intensity. The  $FeCl_2(TMEDA)^+$  ion intensity is attributed to ligand addition of TMEDA to chlorinated  $Fe_2O_3$  on the stainless steel reactor walls.

Ni has three isotopes with significant natural abundances:  $^{58}$ Ni at 100%,  $^{60}$ Ni at 38.2%, and  $^{62}$ Ni at 5.3%. The largest ion intensity of NiCl<sub>2</sub>(TMEDA) is m/z 246 with major contributions from  $^{58}$ Ni $^{35}$ Cl $^{37}$ Cl(TMEDA) and  $^{60}$ Ni $^{35}$ Cl $^{2}$ (TMEDA). The overlapping isotopic signatures of FeCl $^{2}$ (TMEDA) and NiCl $^{2}$ (TMEDA) were calibrated using m/z values unique to the two species: m/z 242 for FeCl $^{2}$ (TMEDA) and m/z 248 for NiCl $^{2}$ (TMEDA). The ion intensity at m/z 248 has contributions from  $^{62}$ Ni $^{35}$ Cl $^{2}$ (TMEDA),  $^{60}$ Ni $^{35}$ Cl $^{37}$ Cl(TMEDA), and  $^{58}$ Ni $^{35}$ Cl $^{2}$ (TMEDA). In spite of the overlap between the Ni and the Fe species, there is still very good agreement between the experimental measurements and calculated ion intensities in Figure 12.

The chlorination of NiO by SO<sub>2</sub>Cl<sub>2</sub> to yield SO<sub>2</sub> is expected based on the reaction

$$NiO + SO_2Cl_2 \rightarrow NiCl_2 + SO_2 + (1/2)O_2$$
 (11)

This reaction is thermochemically favorable with a free energy change of  $\Delta G = -112.0$  kcal/mol at 250 °C. The chlorination of NiO by SO<sub>2</sub>Cl<sub>2</sub> could also yield SO<sub>3</sub> according to

$$NiO + SO_2Cl_2 \rightarrow NiCl_2 + SO_3$$
 (12)

However, this reaction is less thermochemically favorable with a free energy change of  $\Delta G = -77.0$  kcal/mol at 250 °C.

The etching of NiO was also supported by the mass loss of the NiO powder after sequential  $SO_2Cl_2$  and TMEDA exposures. There was a 6.6% mass loss of the NiO powder after 5 cycles of  $SO_2Cl_2$  and TMEDA exposures at 250 °C. This mass loss is lower than the mass losses after 5 cycles of 48.1%, 36.1%, and 31.3% for the CoO,  $Fe_2O_3$ , and ZnO powders, respectively. This smaller mass loss for the NiO powder, along with the lower ion intensity for the NiCl<sub>2</sub>(TMEDA) etch product, indicates a smaller etch rate for NiO using  $SO_2Cl_2$  and TMEDA.

III.D. Other First Row Transition Metal Oxides. Other first row transition metal oxides were also subjected to sequential SO<sub>2</sub>Cl<sub>2</sub> and TMEDA exposures. These metal oxides include TiO<sub>2</sub>, V<sub>2</sub>O<sub>5</sub>, Cr<sub>2</sub>O<sub>3</sub>, MnO<sub>2</sub>, and CuO. No Ti, Cr, or Mn etch species were observed by QMS analysis for TiO<sub>2</sub>, Cr<sub>2</sub>O<sub>3</sub>, or MnO<sub>2</sub> powders at 250 °C. Mass losses for TiO<sub>2</sub>, Cr<sub>2</sub>O<sub>3</sub>, and MnO<sub>2</sub> powder were all less than 4%. These small mass losses can be attributed to losses from sample transfer.

The lack of etching of  $TiO_2$ ,  $Cr_2O_3$ , and  $MnO_2$  can be partially explained by the less favorable thermochemistry for chlorination of these metal oxides. The chlorination reactions and the calculated free energy changes at 250 °C for one mole of  $SO_2Cl_2$  from highest to lowest  $-\Delta G$  values are

\* 
$$ZnO + SO_2Cl_2 \rightarrow ZnCl_2 + SO_2 + (1/2)O_2$$
  
 $\Delta G = -155.6 \text{ kcal/mol}$  (13)

\* CoO + SO<sub>2</sub>Cl<sub>2</sub> 
$$\rightarrow$$
 CoCl<sub>2</sub> + SO<sub>2</sub> + (1/2)O<sub>2</sub>  
 $\Delta G = -136.0 \text{ kcal/mol}$  (14)

\* NiO + SO<sub>2</sub>Cl<sub>2</sub> 
$$\rightarrow$$
 NiCl<sub>2</sub> + SO<sub>2</sub> + (1/2)O<sub>2</sub>  
 $\Delta G = -112.0 \text{ kcal/mol}$  (15)

$$(1/2)\text{TiO}_2 + \text{SO}_2\text{Cl}_2 \rightarrow (1/2)\text{TiCl}_4 + \text{SO}_2 + (1/2)\text{O}_2$$
  
 $\Delta G = -109.8 \text{ kcal/mol}$  (16)

\* 
$$(1/3)\text{Fe}_2\text{O}_3 + \text{SO}_2\text{Cl}_2 \rightarrow (2/3)\text{FeCl}_3 + \text{SO}_2 + (1/2)\text{O}_2$$
  
 $\Delta G = -95.6 \text{ kcal/mol}$  (17)

$$(1/3)$$
Cr<sub>2</sub>O<sub>3</sub> + SO<sub>2</sub>Cl<sub>2</sub>  $\rightarrow$   $(2/3)$ CrCl<sub>3</sub> + SO<sub>2</sub> +  $(1/2)$ O<sub>2</sub>  
 $\Delta G = -85.8$  kcal/mol (18)

$$(1/2)\text{MnO}_2 + \text{SO}_2\text{Cl}_2 \rightarrow (1/2)\text{MnCl}_4 + \text{SO}_2 + (1/2)\text{O}_2$$
  
 $\Delta G = -69.2 \text{ kcal/mol}$  (19)

The metal oxides that etched (CoO, ZnO, Fe<sub>2</sub>O<sub>3</sub>, and NiO indicated by asterisks) predominantly have the larger  $-\Delta G$  values. The metal oxides that did not etch (TiO<sub>2</sub>, Cr<sub>2</sub>O<sub>3</sub>, and MnO<sub>2</sub>) mostly have the smaller  $-\Delta G$  values.

The lack of etching of  $TiO_2$ ,  $Cr_2O_3$ , and  $MnO_2$  can also be partially explained by the less favorable thermochemistry for ligand addition of TMEDA to the various metal chlorides. The reactions for the ligand addition of TMEDA to the various metal chlorides and the calculated free energy changes at 250 °C for one mole of TMEDA from highest to lowest  $-\Delta G$  values are

\* 
$$FeCl_2 + TMEDA \rightarrow FeCl_2(TMEDA)$$
  

$$\Delta G = -88.6 \text{ kcal/mol}$$
(20)

\*  $NiCl_2 + TMEDA \rightarrow NiCl_2(TMEDA)$ 

$$\Delta G = -80.8 \text{ kcal/mol} \tag{21}$$

\*  $ZnCl_2 + TMEDA \rightarrow ZnCl_2(TMEDA)$ 

$$\Delta G = -70.4 \text{ kcal/mol} \tag{22}$$

 $CrCl_3 + TMEDA \rightarrow CrCl_3(TMEDA)$ 

$$\Delta G = -70.1 \text{ kcal/mol} \tag{23}$$

 $MnCl_4 + TMEDA \rightarrow MnCl_4(TMEDA)$ 

$$\Delta G = -59.0 \text{ kcal/mol} \tag{24}$$

\* CoCl<sub>2</sub> + TMEDA  $\rightarrow$  CoCl<sub>2</sub>(TMEDA)

$$\Delta G = -52.6 \text{ kcal/mol} \tag{25}$$

 $TiCl_4 + TMEDA \rightarrow TiCl_4(TMEDA)$ 

$$\Delta G = -39.6 \text{ kcal/mol} \tag{26}$$

The metal oxides that etched (CoO, ZnO, Fe<sub>2</sub>O<sub>3</sub>, and NiO indicated by asterisks) predominantly have the larger  $-\Delta G$  values. Likewise, the metal oxides that did not etch (TiO<sub>2</sub>, Cr<sub>2</sub>O<sub>3</sub>, and MnO<sub>2</sub>) mostly have the lower  $-\Delta G$  values.

 $V_2O_5$  and CuO were unable to be etched in an ALE fashion by sequential  $SO_2Cl_2$  and TMEDA exposures based on self-limiting reactions because they lack a stable chloride. Exposure of  $SO_2Cl_2$  to  $V_2O_5$  and CuO led to the spontaneous thermal etch of  $V_2O_5$  and CuO at 250 °C. Figure 13 shows the ion intensity for  $VOCl_3^+$  during a  $SO_2Cl_2$  exposure on the  $V_2O_5$ 

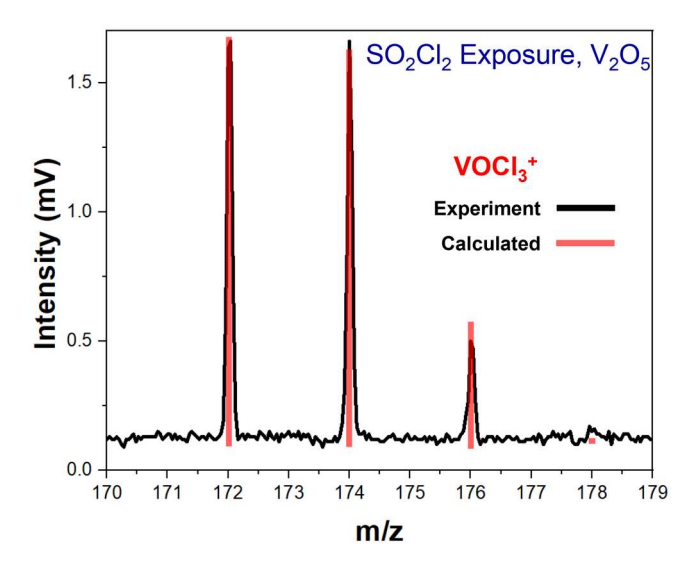


**Figure 13.** Mass spectrum of  $VOCl_3^+$  from  $SO_2Cl_2$  exposure on  $V_2O_5$  at 250 °C. Experimental results are compared with calculated mass spectrum assuming natural isotopic abundances.

powder at 250 °C. The largest ion intensities are for  $VO^{35}Cl_3^+$  and  $VO^{35}Cl_2^{37}Cl^+$  at m/z 172 and 174. There was good agreement between the experimental measurements and the calculated ion intensities based on the natural abundance of the isotopes.

The spontaneous etching of  $V_2O_5$  is explained by the favorability of the chlorination reaction and the volatility of the VOCl<sub>3</sub> chlorination product. The chlorination of  $V_2O_5$  by  $SO_2Cl_2$  to produce VOCl<sub>3</sub> can occur by the reaction

$$V_2O_5 + 3SO_2Cl_2 \rightarrow 2VOCl_3 + 3SO_2 + (3/2)O_2$$
 (27)

This reaction is thermochemically favorable with a free energy change of  $\Delta G = -171.9 \text{ kcal/mol}$  at 250 °C. VOCl<sub>3</sub> would be expected to be extremely volatile because VOCl<sub>3</sub> has a boiling point of 126.7 °C. There was a 31.7% mass loss of the V<sub>2</sub>O<sub>5</sub> powder after exposure to 5 cycles of SO<sub>2</sub>Cl<sub>2</sub> and TMEDA exposures at 250 °C. In addition, no TMEDA metal complexes were observed by QMS analysis.

Spontaneous etching of CuO powder was also observed during  $SO_2Cl_2$  exposures on CuO powder at 250 °C. The  $SO_2Cl_2$  exposure formed volatile  $CuCl_3$ . Figure 14 shows the ion intensities for  $CuCl_3^+$  during an  $SO_2Cl_2$  exposure at 250 °C. The largest ion intensity is for a combination of  $^{63}Cu^{35}Cl_2^{37}Cl^+$  and  $^{65}Cu^{35}Cl_3^+$  at m/z 170. The experimental measurements are in agreement with the calculated intensities based on the natural abundances of the isotopes. The spontaneous etching of CuO powder also led to mass loss. After 5 cycles of  $SO_2Cl_2$  and TMEDA exposures on the CuO powder at 250 °C, there was a 22.8% mass loss of CuO powder.

Although the QMS analysis detects  $CuCl_3^+$  ion intensity,  $CuCl_3$  has not been documented as a product for copper etching. Instead,  $Cu_3Cl_3$  is the reported etch species for Cu etching by chlorine reactants at temperatures between 450 and 590 °C.  $^{50,51}$  At the lower temperature of 250 °C in this work, no cracks of  $Cu_3Cl_3$  were observed up to m/z 500.  $CuCl_3^+$  is also not observed during electron impact ionization of  $Cu_3Cl_3$ . However,  $CuCl_3$  has been reported as the product of an electrochemical atomic layer etch of  $Cu_2S$  by HCl in aqueous solution.  $^{52}$ 

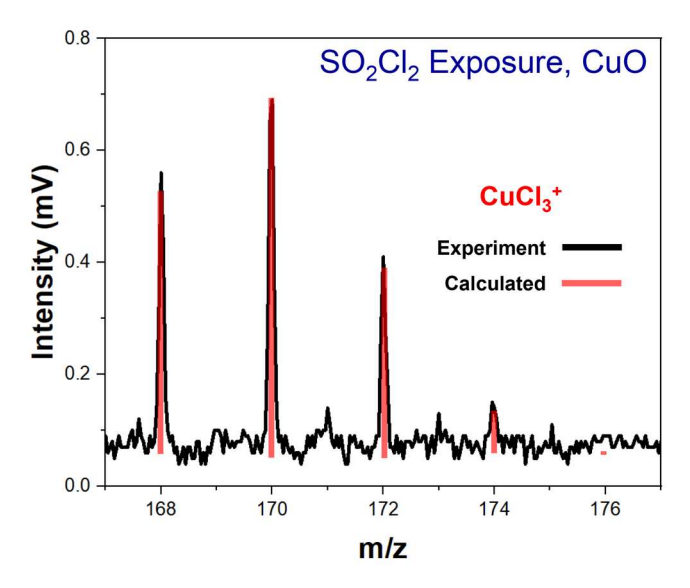


**Figure 14.** Mass spectrum of CuCl<sub>3</sub><sup>+</sup> from SO<sub>2</sub>Cl<sub>2</sub> exposure on CuO at 250 °C. Experimental results are compared with calculated mass spectrum assuming natural isotopic abundances.

In this experiment,  $CuCl_3$  could be formed according to  $CuO + (3/2)SO_2Cl_2 \rightarrow CuCl_3 + (3/2)SO_2 + (1/2)O_2$ (28)

This reaction is thermochemically favorable with a free energy change of  $\Delta G = -161.5$  kcal/mol at 250 °C. Two other potential chlorination reactions to form Cu<sub>3</sub>Cl<sub>3</sub> or CuCl<sub>2</sub> can be expressed as

$$\text{CuO} + \text{SO}_2\text{Cl}_2 \rightarrow (1/3)\text{Cu}_3\text{Cl}_3 + \text{SO}_2 + (1/2)\text{O}_2 + (1/2)\text{Cl}_2$$
(29)

$$CuO + SO_2Cl_2 \rightarrow CuCl_2 + SO_2 + (1/2)O_2$$
 (30)

These two chlorination reactions are less thermochemically favorable with free energy changes at 250 °C of  $\Delta G = -129.2$  kcal/mol for Cu<sub>3</sub>Cl<sub>3</sub> formation and  $\Delta G = -128.9$  kcal/mol for CuCl<sub>2</sub> formation. Consequently, the thermodynamic calculations are consistent with the observed formation of CuCl<sub>3</sub>.

#### IV. CONCLUSIONS

CoO, ZnO, Fe<sub>2</sub>O<sub>3</sub>, and NiO were thermally etched at 250  $^{\circ}$ C using sequential chlorination and ligand-addition reactions. The chlorination of these first-row transition metal oxides was accomplished using SO<sub>2</sub>Cl<sub>2</sub>. The subsequent ligand-addition reaction was performed using TMEDA. *In situ* QMS studies revealed that ligand addition on the metal chloride was able to form volatile MCl<sub>2</sub>(TMEDA) complexes. The QMS analysis revealed that CoCl<sub>2</sub>(TMEDA)<sup>+</sup>, ZnCl(TMEDA)<sup>+</sup>, FeCl<sub>2</sub>(TMEDA)<sup>+</sup>, and NiCl<sub>2</sub>(TMEDA)<sup>+</sup> ion intensities were detected during TMEDA exposures on the chlorinated CoO, ZnO, Fe<sub>2</sub>O<sub>3</sub>, and NiO substrates, respectively.

The QMS analysis was able to monitor the time dependence of the chlorination and ligand-addition reaction. The production of  $SO_2$  was suggested by the appearance of a peak in the  $SO_2^+$  ion intensity at the beginning of the  $SO_2Cl_2$  exposure. The peak in the  $SO_2^+$  intensity coincided with an absence of signal from the  $SO_2Cl_2^+$  ion intensity. The time-dependence of the  $SO_2^+$  and  $SO_2Cl_2^+$  ion intensities was consistent with  $SO_2Cl_2$  chlorinating the metal oxide to produce  $SO_2$ . During the TMEDA exposures, the ion intensity for

 $MCl_2(TMEDA)^+$  peaked at the beginning of the TMEDA exposures. The subsequent decay of the  $MCl_2(TMEDA)^+$  ion intensity while the  $(TMEDA)^+$  ion intensity remained constant was evidence for a self-limiting ligand-addition reaction.

Additional experiments on flat substrates provided evidence for the etching of the metal oxides during sequential  $SO_2Cl_2$  and TMEDA exposures. For CoO thermal ALE, an etch rate of 4.1 Å/cycle at 250 °C was determined from XRR studies. For ZnO thermal ALE, an etch rate of 0.12 Å/cycle at 250 °C was determined using QCM investigations. The loss of mass during sequential  $SO_2Cl_2$  and TMEDA exposures was also confirmed by measurements on the CoO, ZnO, Fe<sub>2</sub>O<sub>3</sub>, and NiO powders.

In contrast, QMS studies of  $TiO_2$ ,  $Cr_2O_3$ , and  $MnO_2$  displayed no volatile species formation during sequential  $SO_2Cl_2$  and TMEDA exposures at 250 °C. The lack of etching was attributed to the less thermochemically favorable chlorination of these metal oxides by  $SO_2Cl_2$  and the less thermochemically favorable ligand addition of TMEDA to the corresponding metal chlorides.  $TiO_2$ ,  $Cr_2O_3$ , and  $MnO_2$  had calculated  $-\Delta G$  values for chlorination and ligand addition that were mostly smaller than the  $-\Delta G$  values for CoO, ZnO,  $Fe_2O_3$ , and NiO. Self-limiting thermal ALE reactions could not be achieved on  $V_2O_5$  and CuO because these metal oxides were spontaneously etched using  $SO_2Cl_2$  at 250 °C. The QMS analysis detected volatile VOCl<sub>3</sub> and CuCl<sub>3</sub> etch products for  $V_2O_5$  and CuO, respectively.

These investigations indicate that sequential chlorination and ligand-addition reactions with  $SO_2Cl_2$  and TMEDA can provide a useful pathway for the thermal ALE of a variety of first-row transition metal oxides. Sequential chlorination and ligand-addition reactions will be particularly useful for the thermal ALE of metal oxides that have associated metal fluorides that are not easily volatilized by ligand-exchange reactions. The chlorination and ligand-addition reaction pathway should provide a valuable complement to the fluorination and ligand-exchange mechanism.

#### AUTHOR INFORMATION

#### **Corresponding Author**

**Steven M. George** – Department of Chemistry, University of Colorado, Boulder, Colorado 80309, United States;

o orcid.org/0000-0003-0253-9184; Email: steven.george@colorado.edu

#### **Authors**

Jonathan L. Partridge — Department of Chemistry, University of Colorado, Boulder, Colorado 80309, United States;
orcid.org/0000-0002-0071-9854

**Jessica A. Murdzek** – Department of Chemistry, University of Colorado, Boulder, Colorado 80309, United States

Virginia L. Johnson – Department of Chemistry, University of Colorado, Boulder, Colorado 80309, United States

Andrew S. Cavanagh — Department of Chemistry, University of Colorado, Boulder, Colorado 80309, United States;
orcid.org/0000-0002-6201-530X

Andreas Fischer – Lam Research Corporation, Fremont, California 94538, United States

Thorsten Lill – Lam Research Corporation, Fremont, California 94538, United States

Sandeep Sharma – Department of Chemistry, University of Colorado, Boulder, Colorado 80309, United States

Complete contact information is available at: https://pubs.acs.org/10.1021/acs.chemmater.2c03616

#### Notes

The authors declare no competing financial interest.

#### ACKNOWLEDGMENTS

This research was funded by the Lam Research Corporation. The authors thank Greg Their at Extrel for the molecular beam design and installation of the QMS. The authors also acknowledge Kenneth Smith, Donald David, and the CIRES/Chemistry Integrated Instrument Development Facility at the University of Colorado for their help in the design and construction of the new reactor. This work utilized the Blanca condo computing resource at the University of Colorado Boulder. Blanca is jointly funded by computing users and the University of Colorado Boulder. V.L.J. was supported by an NSF Graduate Research Fellowship under Grant DGE-2040434. S.S. was supported by NSF Grant CHE-2145209.

#### REFERENCES

- (1) Fischer, A.; Routzahn, A.; George, S. M.; Lill, T. Thermal Atomic Layer Etching: A Review. *J. Vac. Sci. Technol. A* **2021**, 39, 030801.
- (2) Kanarik, K. J.; Lill, T.; Hudson, E. A.; Sriraman, S.; Tan, S.; Marks, J.; Vahedi, V.; Gottscho, R. A. Overview of Atomic Layer Etching in the Semiconductor Industry. *J. Vac. Sci. Technol. A* **2015**, 33, 020802.
- (3) George, S. M. Mechanisms of Thermal Atomic Layer Etching. *Acc. Chem. Res.* **2020**, 53, 1151–1160.
- (4) Lee, Y.; George, S. M. Atomic Layer Etching of  $Al_2O_3$  Using Sequential, Self-limiting Thermal Reactions with  $Sn(acac)_2$  and Hydrogen Fluoride. *ACS Nano* **2015**, *9*, 2061–2070.
- (5) George, S. M.; Lee, Y. Prospects for Thermal Atomic Layer Etching Using Sequential, Self-Limiting Fluorination and Ligand-Exchange Reactions. *ACS Nano* **2016**, *10*, 4889–4894.
- (6) Cano, A. M.; Marquardt, A. E.; DuMont, J. W.; George, S. M. Effect of HF Pressure on Thermal Al<sub>2</sub>O<sub>3</sub> Atomic Layer Etch Rates and Al<sub>2</sub>O<sub>3</sub> Fluorination. *J. Phys. Chem. C* **2019**, *123*, 10346–10355.
- (7) Clancey, J. W.; Cavanagh, A. S.; Smith, J. E. T.; Sharma, S.; George, S. M. Volatile Etch Species Produced during Thermal Al<sub>2</sub>O<sub>3</sub> Atomic Layer Etching. *J. Phys. Chem. C* **2020**, *124*, 287–299.
- (8) Lii-Rosales, A.; Cavanagh, A. S.; Fischer, A.; Lill, T.; George, S. M. Spontaneous Etching of Metal Fluorides Using Ligand-Exchange Reactions: Landscape Revealed by Mass Spectrometry. *Chem. Mater.* **2021**, 33, 7719–7730.
- (9) Lii-Rosales, A.; Johnson, V. L.; Cavanagh, A. S.; Fischer, A.; Lill, T.; Sharma, S.; George, S. M. Effectiveness of Different Ligands on Silane Precursors for Ligand Exchange to Etch Metal Fluorides. *Chem. Mater.* **2022**, *34*, 8641–8653.
- (10) Lee, Y.; DuMont, J. W.; George, S. M. Trimethylaluminum as the Metal Precursor for the Atomic Layer Etching of  $Al_2O_3$  Using Sequential, Self-Limiting Thermal Reactions. *Chem. Mater.* **2016**, 28, 2994–3003
- (11) Lee, Y.; George, S. M. Thermal Atomic Layer Etching of  $Al_2O_3$ ,  $HfO_2$ , and  $ZrO_2$  Using Sequential Hydrogen Fluoride and Dimethylaluminum Chloride Exposures. J. Phys. Chem. C **2019**, 123, 18455–18466.
- (12) Lee, Y.; Huffman, C.; George, S. M. Selectivity in Thermal Atomic Layer Etching Using Sequential, Self Limiting Fluorination and Ligand-Exchange Reactions. *Chem. Mater.* **2016**, 28, 7657–7665.
- (13) Lee, Y.; George, S. M. Thermal Atomic Layer Etching of HfO<sub>2</sub> Using HF for Fluorination and TiCl<sub>4</sub> for Ligand Exchange. *J. Vac. Sci. Technol. A* **2018**, *36*, 061504.
- (14) Johnson, N. R.; George, S. M. WO<sub>3</sub> and W Thermal Atomic Layer Etching Using "Conversion-Fluorination" and "Oxidation-Conversion-Fluorination" Mechanisms. *ACS Appl. Mater. Interfaces* **2017**, *9*, 34435–34447.
- (15) Cano, A. M.; Kondati Natarajan, S.; Partridge, J. L.; Elliott, S. D.; George, S. M. Spontaneous Etching of B<sub>2</sub>O<sub>3</sub> by HF Gas Studied

- Using Infrared Spectroscopy, Mass Spectrometry, and Density Functional Theory. J. Vac. Sci. Technol. A 2022, 40, 022601.
- (16) Myers, T. J.; Cano, A. M.; Lancaster, D. K.; Clancey, J. W.; George, S. M. Conversion Reactions in Atomic Layer Processing with Emphasis on ZnO Conversion to Al<sub>2</sub>O<sub>3</sub> by Trimethylaluminum. *J. Vac. Sci. Technol. A* **2021**, 39, 021001.
- (17) DuMont, J. W.; Marquardt, A. E.; Cano, A. M.; George, S. M. Thermal Atomic Layer Etching of  ${\rm SiO_2}$  by a "Conversion-Etch" Mechanism Using Sequential Reactions of Trimethylaluminum and Hydrogen Fluoride. ACS Appl. Mater. Interfaces 2017, 9, 10296—10307.
- (18) Zywotko, D. R.; George, S. M. Thermal Atomic Layer Etching of ZnO by a "Conversion-Etch" Mechanism Using Sequential Exposures of Hydrogen Fluoride and Trimethylaluminum. *Chem. Mater.* **2017**, 29, 1183–1191.
- (19) Abdulagatov, A. I.; George, S. M. Thermal Atomic Layer Etching of Silicon Using  $O_2$ , HF, and  $Al(CH_3)_3$  as the Reactants. *Chem. Mater.* **2018**, 30, 8465–8475.
- (20) Abdulagatov, A. I.; George, S. M. Thermal Atomic Layer Etching of Silicon Nitride Using an Oxidation and "Conversion Etch" Mechanism. *J. Vac. Sci. Technol. A* **2020**, *38*, 022607.
- (21) Abdulagatov, A. I.; Sharma, V.; Murdzek, J. A.; Cavanagh, A. S.; George, S. M. Thermal Atomic Layer Etching of Germanium-rich SiGe Using an Oxidation and "Conversion-Etch" Mechanism. *J. Vac. Sci. Technol. A* **2021**, *39*, 022602.
- (22) Lee, Y.; George, S. M. Thermal Atomic Layer Etching of Titanium Nitride Using Sequential, Self-Limiting Reactions: Oxidation to  $TiO_2$  and Fluorination to Volatile  $TiF_4$ . Chem. Mater. 2017, 29, 8202–8210.
- (23) Kondati Natarajan, S.; Cano, A. M.; Partridge, J. L.; George, S. M.; Elliott, S. D. Prediction and Validation of the Process Window for Atomic Layer Etching: HF Exposure on TiO<sub>2</sub>. *J. Phys. Chem. C* **2021**, 125, 25589–25599.
- (24) Chen, J. K. C.; Altieri, N. D.; Kim, T.; Chen, E.; Lill, T.; Shen, M. H.; Chang, J. P. Directional Etch of Magnetic and Noble Metals. II. Organic Chemical Vapor Etch. *J. Vac. Sci. Technol. A* **2017**, *35*, 05c305.
- (25) Konh, M.; He, C.; Lin, X.; Guo, X. Y.; Pallem, V.; Opila, R. L.; Teplyakov, A. V.; Wang, Z. J.; Yuan, B. Molecular Mechanisms of Atomic Layer Etching of Cobalt with Sequential Exposure to Molecular Chlorine and Diketones. *J. Vac. Sci. Technol. A* **2019**, 37, 021004.
- (26) Mohimi, E.; Chu, X. Q. I.; Trinh, B. B.; Babar, S.; Girolami, G. S.; Abelson, J. R. Thermal Atomic Layer Etching of Copper by Sequential Steps Involving Oxidation and Exposure to Hexafluor-oacetylacetone. ECS J. Solid State Sci. Technol. 2018, 7, P491–P495.
- (27) Murdzek, J. A.; Lii-Rosales, A.; George, S. M. Thermal Atomic Layer Etching of Nickel Using Sequential Chlorination and Ligand-Addition Reactions. *Chem. Mater.* **2021**, *33*, 9174–9183.
- (28) Lii-Rosales, A.; Johnson, V. L.; Sharma, S.; Fischer, A.; Lill, T.; George, S. M. Volatile Products from Ligand Addition of P(CH<sub>3</sub>)<sub>3</sub> to NiCl<sub>2</sub>, PdCl<sub>2</sub>, and PtCl<sub>2</sub>: Pathway for Metal Thermal Atomic Layer Etching. *J. Phys. Chem. C* **2022**, *126*, 8287–8295.
- (29) Chen, J. K. C.; Kim, T.; Altieri, N. D.; Chen, E.; Chang, J. P. Ion Beam Assisted Organic Chemical Vapor Etch of Magnetic Thin Films. *J. Vac. Sci. Technol. A* **2017**, *35*, 031304.
- (30) Kim, J. E.; Kim, D. S.; Gill, Y. J.; Jang, Y. J.; Kim, Y. E.; Cho, H.; Won, B. Y.; Kwon, O.; Yoon, K.; Choi, J. Y.; et al. Etch Characteristics of Magnetic Tunnel Junction Materials Using H<sub>2</sub>/NH<sub>3</sub> Reactive Ion Beam. *Nanotechnology* **2021**, *32*, 055301.
- (31) Raha, S.; Ahmaruzzaman, M. ZnO Nanostructured Materials and their Potential Applications: Progress, Challenges and Perspectives. *Nanoscale Adv.* **2022**, *4*, 1868–1925.
- (32) Väyrynen, K.; Hatanpää, T.; Mattinen, M.; Heikkilä, M.; Mizohata, K.; Meinander, K.; Räisänen, J.; Ritala, M.; Leskelä, M. Diamine Adduct of Cobalt(II) Chloride as a Precursor for Atomic Layer Deposition of Stoichiometric Cobalt(II) Oxide and Reduction Thereof to Cobalt Metal Thin Films. *Chem. Mater.* **2018**, *30*, 3499–3507.

- (33) Elam, J. W.; Groner, M. D.; George, S. M. Viscous Flow Reactor with Quartz Crystal Microbalance for Thin Film Growth by Atomic Layer Deposition. *Rev. Sci. Instrum.* **2002**, *73*, 2981–2981.
- (34) Frisch, M. J.; Trucks, G. W.; Schlegel, H. B.; Scuseria, G. E.; Robb, M. A.; Cheeseman, J. R.; Scalmani, G.; Barone, V.; Petersson, G. A.; Nakatsuji, H.; et al. *Gaussian 16*, Rev. B.01; Gaussian Inc.: Wallingford, CT, 2016.
- (35) Dunning, T. H., Jr.; Hay, P. J. In Methods of Electronic Structure Theory; Schaefer, H. F., Ed.; Springer Science: New York, 1977.
- (36) Lee, C.; Yang, W.; Parr, R. G. Development of the Colle-Salvetti Correlation-Energy Formula into a Functional of the Electron Density. *Phys. Rev. B* **1988**, *37*, 785–789.
- (37) Scuseria, G. E.; Janssen, C. L.; Schaefer, H. F. An Efficient Reformulation of the Closed-Shell Coupled Cluster Single and Double Excitation (CCSD) Equations. *J. Chem. Phys.* **1988**, *89*, 7382–7387.
- (38) Scuseria, G. E.; Schaefer, H. F. Is Coupled Cluster Singles and Doubles (CCSD) Mmore Computationally Intensive than Quadratic Configuration Interaction (QCISD)? *J. Chem. Phys.* **1989**, 90, 3700–3703
- (39) Weigend, F.; Ahlrichs, R. Balanced Basis Sets of Split Valence, Triple Zeta Valence and Quadruple Zeta Valence Quality for H to Rn: Design and Assessment of Accuracy. *Phys. Chem. Chem. Phys.* **2005**, *7*, 3297–3305.
- (40) Munson, B.; Smith, D.; Polley, C. The Mass Spectrum, Proton Affinity, and Ion–Molecule Reactions of SO<sub>3</sub>. *Int. J. Mass Spectrom. Ion Phys.* **1977**, 25, 323–326.
- (41) Cotton, F. A.; Wilkinson, G.; Murillo, C. A.; Bochmann, M. *Advanced Inorganic Chemistry*, 6th ed.; John Wiley & Sons: New York, 1999.
- (42) Khadka, C. B.; Eichhöfer, A.; Weigend, F.; Corrigan, J. F. Zinc Chalcogenolate Complexes as Precursors to ZnE and Mn/ZnE (E = S, Se) Clusters. *Inorg. Chem.* **2012**, *51*, 2747–2756.
- (43) Bal-Demirci, T. Synthesis, Spectral Characterization of the Zinc(II) Mixed-ligand Complexes of N(4)-allyl Thiosemicarbazones and N,N,N',N'-Tetramethylethylenediamine, and Crystal Structure of the Novel [ZnL<sub>2</sub>(tmen)] Compound. *Polyhedron* **2008**, 27, 440–446.
- (44) Htoon, S.; Ladd, M. Crystallographic Studies of Dihalogeno-Tetramethylethylenediamine Complexes of Zinc, Cadmium and Mercury. I: Crystal and Molecular Structure of Dichloro-(N,N,N',N'-tetramethylethylenediamine)zinc(II). *J. Crys. Mol. Struct.* 1973, 3, 95–102.
- (45) Au-Yeung, H. Y.; Lam, C. H.; Lam, C.-K.; Wong, W.-Y.; Lee, H. K. Unusual Iron(II) and Cobalt(II) Complexes Derived from Monodentate Arylamido Ligands. *Inorg. Chem.* **2007**, *46*, 7695–7697.
- (46) Davies, S. C.; Hughes, D. L.; Leigh, G. J.; Sanders, J. R.; De Souza, J. S. Mono-, Di-, and Tri-Nuclear Complexes of Iron(II) with N,N,N,N-tetra-methylethylenediamine. *J. Chem. Soc., Dalton Trans.* 1997, No. 11, 1981–1988.
- (47) Sacconi, L.; Bertini, I.; Mani, F. Metal Complexes of N,N,N',N'-Tetramethyldiamines. I. Nickel(II) and Cobalt(II) Complexes. *Inorg. Chem.* **1967**, *6*, 262–267.
- (48) Miyamoto, K.; Sakamoto, M.; Tanaka, C.; Horn, E.; Fukuda, Y. Syntheses, Structures, Spectroscopic Properties, and Thermal Behavior of Nickel(II) Mixed-Ligand Complexes with N,N,N',N'-Tetramethylethylenediamine, Benzoylacetonate, and a Halide Anion. *Bull. Chem. Soc. Jpn.* **2005**, *78*, 1061–1071.
- (49) Shields, J. D.; Gray, E. E.; Doyle, A. G. A Modular, Air-Stable Nickel Precatalyst. Org. Lett. 2015, 17, 2166-2169.
- (50) Winters, H. F. Etch Products from the Reaction on Cl<sub>2</sub> with Al(100) and Cu(100) and XeF<sub>2</sub> with W(111) and Nb. *J. Vac. Sci. Technol. B* **1985**, 3, 9–15.
- (51) Altieri, N. D.; Chen, J. K.-C.; Minardi, L.; Chang, J. P. Plasma—Surface Interactions at the Atomic Scale for Patterning Metals. *J. Vac. Sci. Technol. A* **2017**, *35*, 05C203.
- (52) Gong, Y.; Venkatraman, K.; Akolkar, R. Electrochemical Atomic Layer Etching of Copper. *J. Electrochem. Soc.* **2018**, *165*, D282–D284.

### **□** Recommended by ACS

#### Thermal Atomic Layer Etching of MoS<sub>2</sub> Using MoF<sub>6</sub> and H<sub>2</sub>O

Jake Soares, Elton Graugnard, et al.

JANUARY 12, 2023

CHEMISTRY OF MATERIALS

READ 🗹

# Tungsten Carbide Nanolayer Formation by Ion Beam Mixing with Argon and Xenon Ions for Applications as Protective Coatings

Adel Sarolta Racz, Miklos Menyhard, et al.

FEBRUARY 22, 2023

ACS APPLIED NANO MATERIALS

READ 🗹

## Defect-Dependent Surface Phase Transformation on 1T-TiS $_2$ Assisted by Water

Xue Chen, Liang Cao, et al.

FEBRUARY 08, 2023

THE JOURNAL OF PHYSICAL CHEMISTRY C

READ 🗹

#### High Field-Effect Mobility and On/Off Current Ratio of p-Type ALD SnO Thin-Film Transistor

Myeong Gil Chae, Jeong Hwan Han, et al.

FEBRUARY 03, 2023

ACS APPLIED ELECTRONIC MATERIALS

READ 🗹

Get More Suggestions >